Article

Claudin-11 Tight Junctions in Myelin Are a Barrier to Diffusion and Lack Strong Adhesive Properties

Andrew R. Denninger,[1] Andrew Breglio,[1] Kathleen J. Maheras,[4] Geraldine LeDuc,[5] Viviana Cristiglio,[6] Bruno Demé,[6] Alexander Gow,[2,3,4] and Daniel A. Kirschner[1,*]

[1]Biology Department, Boston College, Chestnut Hill, Massachusetts; [2]Center for Molecular Medicine and Genetics, [3]Carman and Ann Adams Department of Pediatrics, and [4]Department of Neurology, Wayne State University School of Medicine, Detroit, Michigan; [5]European Synchrotron Radiation Facility, Grenoble, France; and [6]Institut Laue-Langevin, Grenoble, France

ABSTRACT The radial component is a network of interlamellar tight junctions (TJs) unique to central nervous system myelin. Ablation of claudin-11, a TJ protein, results in the absence of the radial component and compromises the passive electrical properties of myelin. Although TJs are known to regulate paracellular diffusion, this barrier function has not been directly demonstrated for the radial component, and some evidence suggests that the radial component may also mediate adhesion between myelin membranes. To investigate the physical properties of claudin-11 TJs, we compared fresh, unfixed *Claudin 11*-null and control nerves using x-ray and neutron diffraction. In *Claudin 11*-null tissue, we detected no changes in myelin structure, stability, or membrane interactions, which argues against the notion that myelin TJs exhibit significant adhesive properties. Moreover, our osmotic stressing and D_2O-H_2O exchange experiments demonstrate that myelin lacking claudin-11 is more permeable to water and small osmolytes. Thus, our data indicate that the radial component serves primarily as a diffusion barrier and elucidate the mechanism by which TJs govern myelin function.

INTRODUCTION

The myelin sheath is a multilamellar assembly of lipid-rich membranes that surrounds nerve axons. This high-resistance, low-capacitance insulation inhibits current flow across the internodal axolemma and restricts the generation of action potentials to the nodes of Ranvier, allowing for rapid signal propagation down the length of the axon via saltatory conduction. Myelin's ability to accelerate the transmission of nerve impulses depends both on its own intrinsic biophysical properties as well as on its intimate relationship with the underlying axon, specifically in the paranodal and juxtaparanodal regions where axo-glial junctions maintain the spatial organization of axonal ion channels. Although much is understood about the role of the axo-glial junctions in nerve physiology, relatively little is known about how the interlamellar tight junctions (TJs), or radial component, of internodal myelin in the central nervous system (CNS) contribute to myelin properties and function (1,2).

The radial component of CNS myelin was first observed in cross sections of optic nerves where it appears as radially oriented, linear arrays of thickenings of the intraperiod line extending across the myelin sheath (3,4). Because the radial component bears a striking resemblance to previously characterized TJs, many hypothesized that it too might possess barrier properties. Although the barrier function of other TJs had been clearly demonstrated (5–7), direct experimental support for the tightness of myelin TJs was elusive. Electron microscopic studies of the permeability of both central and peripheral nervous system myelin were difficult to interpret because of the uneven infiltration of diffusion tracers, the inconsistent methods used among studies, the poor temporal resolution inherent to transmission electron microscopy (TEM), and preparatory artifacts (8–22). Concurrently, other groups proposed that the radial component instead, or in addition, had adhesive properties, which is not a primary function of canonical TJs. For example, when CNS myelin is treated with either hypotonic solutions (23) or hexachlorophene (18) to induce decompaction of the multilamellar arrays, regions of the sheath containing the radial component tend to remain compacted.

The identification of claudin-11, a member of the claudin family of transmembrane TJ proteins, as an essential constituent of the radial component provided the opportunity to directly test the function of interlamellar TJs in CNS myelin (1,24). Mice lacking *Claudin 11* (*Cldn11*) suffer from mild tremors, gait abnormalities, motor defects, and electrophysiological abnormalities, including a 50% decrease in conduction velocity in small diameter axons (1,2,25,26). Nonetheless, CNS myelin in *Cldn11*-null mice is ultrastructurally normal (aside from the conspicuous absence of the radial component), suggesting that the primary function of claudin-11 is the formation of a diffusion barrier rather than the provision of mechanical stability. Indeed, modeling of the electrophysiology data from these

Submitted June 2, 2015, and accepted for publication August 11, 2015.

*Correspondence: kirschnd@bc.edu

Editor: Lois Pollack.

0006-3495/15/10/1387/11

http://dx.doi.org/10.1016/j.bpj.2015.08.012

mice suggests that their nervous system deficits are consistent with an increase in current flow through the sheath (2). Additional work has shown that claudin-11 is involved in the formation of barriers elsewhere in the body, including between Sertoli cells of the testes and between basal cells in the stria vascularis of the cochlear duct, where its absence causes no primary defects in cell adhesion (1,24,27–29). Combined, these results strongly suggest that the *Cldn11*-null CNS phenotype results from the loss of a diffusion barrier within myelin rather than the loss of adhesion, but this mechanism has yet to be demonstrated directly.

To examine the function of claudin-11 in the myelin sheath, we used x-ray and neutron diffraction to compare myelin structure and permeability in unfixed, myelinated tissues from claudin-11-deficient and control mice. We found that the period, amount, structure, and stability of CNS myelin were indistinguishable between *Cldn11*-null and control mice. By contrast, measurements of the exchange kinetics for water and small nonelectrolytes revealed increased rates of diffusion in *Cldn11*-null myelin. These results provide the first, to our knowledge, direct evidence for the barrier function provided by claudin-11 in myelin and reveal the fundamental importance of TJs in the maintenance of myelin's insulative properties.

MATERIALS AND METHODS

Specimens

Cldn11-null, heterozygous, and wild-type (WT) mice were generated, genotyped, and maintained at Wayne State University as previously described (1). For all experiments, littermates were used when possible; otherwise, age-matched mice were obtained from multiple sibling breeder pairs. Mice were 4–12 months old. For x-ray diffraction (XRD) experiments, mice were transported to the Boston College Animal Care Facility. Optic and sciatic nerves were isolated from animals that had been sacrificed using cervical dislocation. Nerves were tied off at both ends with silk suture and maintained in phosphate-buffered saline (PBS) (5 mM sodium phosphate, 154 mM NaCl, pH 7.4) until subsequent analysis. For neutron diffraction experiments, the mice were transported from Wayne State University to Grenoble, France, where they were housed at the Biomedical Facility at the European Synchrotron Radiation Facility. Spinal cords and sciatic nerves were isolated from mice that had been sacrificed using isoflurane followed by decapitation. Spinal cords were bisected sagittally before analysis. Samples were tied off at both ends with silk suture and maintained in Tris-buffered saline (5 mM Tris base, 154 mM NaCl, pH/pD 7.4) of varying D_2O content (0–100%) until subsequent analysis. The knots on spinal cord segments were typically stabilized using cyanoacrylate adhesive because of the delicate nature of the tissue. All animal procedures were conducted in accordance with protocols approved by the Institutional Animal Care and Use Committees at Wayne State University, Boston College, and the European Synchrotron Radiation Facility.

XRD

XRD experiments were performed as previously described (30) using nickel-filtered, single-mirror focused CuKα radiation from a fine-line source on a 3.0 kW Rigaku x-ray generator operated at 40 kV by 10 mA. Diffraction patterns were collected using a linear, position-sensitive detector (Molecular Metrology, Northampton, MA). For static experiments, nerves were equilibrated against PBS, loaded into thin-walled, quartz capillaries containing the same solution, and sealed with wax and enamel. Exposure times were 30 min. For electrostatic stressing experiments, nerves were first equilibrated against either PBS or acetate-buffered saline (pH 4) with enough sodium chloride to reach the desired ionic strength (0.02, 0.06, 0.15, or 0.2) and then loaded into a capillary containing the same solution. For some osmotic stressing experiments, nerves were incubated in bulk PBS containing an osmolyte of interest and loaded into a capillary containing the same solution. For osmotic stressing kinetics experiments, the sample was loaded into a thin-walled, quartz capillary tube (inner diameter, 1.0 mm) that had been epoxied into an aluminum yoke. The suture tied to the ends of the sample was attached to stainless steel pins on each side of the yoke using small O-rings to hold the sample in place. The sample yoke was placed inside a Lucite perfusion yoke and sealed with O-rings. The outer yoke was connected to a peristaltic pump and a buffer reservoir with Tygon tubing. The peristaltic pump continuously replaced the fluid surrounding the sample at a flow rate of 2.5 mL/min. A series of tandem 1-min exposures was collected for at least 4 h while the sample was flushed with a hypertonic solution, 1 M sucrose in PBS. XRD patterns were analyzed using PeakFit (Systat Software, San Jose, CA). Myelin period (d) was calculated from the positions of the intensity maxima in the diffraction patterns. The relative amount of myelin ($M/[M+B]$) was calculated by comparing the integrated intensity of all maxima to total scatter, including background and excluding small-angle scatter around the beamstop and wide-angle scatter (30).

Neutron diffraction

Neutron diffraction experiments were carried out on the D16 instrument at the Institut Laue-Langevin (Grenoble, France) as previously described (31). To optimize sample illumination and angular resolution in the horizontal direction, we used a beam size of 2 mm (horizontal) $\times$ 15 mm (vertical). Neutron wavelength was 4.75 Å. Diffraction patterns were collected using the Millimeter Resolution Large Area Neutron Detector (MiLAND), a high pressure ^{3}He neutron detector with an area of 320 mm $\times$ 320 mm and a pixel resolution of 1 mm $\times$ 1 mm. The sample-to-detector distance was 870 mm. All neutron diffraction experiments were performed at ambient temperature and pressure. For static measurements, samples were loaded into thin-walled, quartz capillary tubes (Charles Supper Company, Natick, MA) filled with Tris-buffered saline containing a known fraction of D_2O and sealed with wax and enamel. Exposure times in static experiments ranged from 1 to 5 h. For H_2O-D_2O exchange experiments, the sample to be perfused was loaded into a Suprasil EPR tube (Wilmad-LabGlass, Vineland, NJ; inner diameter, 2 mm; outer diameter, 3 mm) that had been epoxied into an aluminum or Lucite yoke. The suture tied to the ends of the sample was attached to stainless steel pins on each side of the yoke to hold the sample in place. The sample yoke was placed inside a Lucite perfusion yoke and sealed with O-rings. The outer yoke was connected to a peristaltic pump and a buffer reservoir with Tygon tubing. The peristaltic pump continuously replaced the fluid surrounding the sample at a flow rate of 0.5 mL/s.

Diffraction data for H_2O-D_2O exchange experiments were collected as a tandem series of increasingly long exposures—5, 10, 15, 30 s, and 1 min for a total exposure of $>$1 h. The detector was positioned so that it could detect a range in R from -0.018 Å^{-1} to 0.59 Å^{-1}, which included the direct beam and each of the two second-order reflections near ± 0.013 Å^{-1} (CNS). This allowed for high counting statistics during the short exposure times used for exchange experiments through the integration of the pair of unique second-order reflections. We used a neutron-translucent, 250 μm-thick, cadmium beamstop to attenuate the transmitted direct beam and allow for transmission measurements during data acquisition.

Neutron data refinement

Data refinement was performed as previously described (31) using the ILL in-house software LAMP (32). Briefly, diffraction patterns were first

normalized to incident neutron beam flux to correct for differences in beam intensity and exposure time. Second, they were corrected for pixel efficiency and solid angle by normalizing to a detector calibration file containing the flat incoherent signal from water. They were then corrected for the attenuation of the incident beam by the sample (transmission). Finally, background patterns from empty Suprasil EPR tubes or quartz capillaries were subtracted from each pattern. The corrected patterns were integrated azimuthally along the fiber axis to produce one-dimensional diffraction patterns. Peak positions, widths, and intensities above background were measured from the resulting patterns using either LAMP or PeakFit. For all samples, the integrated intensity of the fourth-order reflection was corrected to remove the contribution of the doubly scattered second-order reflection (33). Corrected peak intensities (I_h) of Bragg order h were then converted to structure factor amplitudes ($|F_h|$). To correct for small differences in sample size and orientation, second-order structure factors were linearized versus $\%D_2O$ and normalized to unity at 100% D_2O. Remaining structure factors were scaled based on the relative amplitudes of their $|F_2|$ to the expected $|F_2|$ at that $\%D_2O$.

RESULTS

Myelin structure and amount are normal in *Cldn11*-null mice

To determine whether the absence of claudin-11 causes any defects in myelin structure, we analyzed myelin in optic nerves isolated from WT (+/+), heterozygous (+/−), and *Cldn11*-null (−/−) mice using XRD. As indicated by the similarity of scattered x-ray intensity and peak positions among samples from all genotypes (Fig. 1 *A*), the absence of claudin-11 had no significant effects on either the relative amount of myelin or myelin period (Fig. 1 *B* and Table 1), respectively. Sciatic nerves, which do not contain claudin-11, were analyzed as internal controls and showed no differences between the three genotypes.

To examine whether the absence of claudin-11 has more subtle effects on myelin structure, we normalized the intensity of the observed reflections (I_h) to the intensity of the second-order reflection (I_2) and compared these relative intensities (I_h/I_2) between genotypes. Differences in these relative intensities would indicate differences in the distribution of electron density across myelin's repeating unit (a pair of membrane bilayers). In optic nerves, we found that I_4/I_2 was indistinguishable between genotypes (Fig. 2 *A* and Table 1). Similarly, we found no differences between the relative intensities of I_1 through I_5 in sciatic nerves.

As a further test for defects in myelin structure, we measured the widths of the observed reflections, which is an indicator of the regularity of membrane packing. The slope of a linear regression between the square of the full width at half-maximum (w_h^2) and the fourth power of the Bragg order (h^4) for each reflection is directly related to the amount of disorder in membrane packing, whereas the intercept is inversely proportional to the regularity (crystallinity; coherence length, or average number of layers) of membrane packing (34). We found that packing disorder and crystallinity in myelin were similar across genotypes

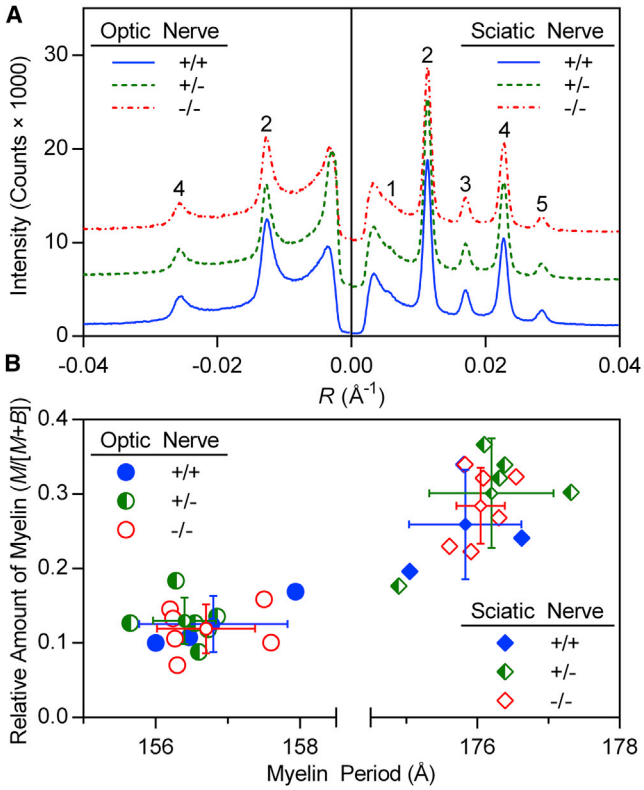

FIGURE 1 Myelin period and amount are unaffected in *Cldn11*-null mice. (*A*) Representative XRD patterns collected from optic nerves (*left*) and sciatic nerves (*right*) from WT (+/+; $n = 3$), heterozygous (+/−; $n = 6$), and *Cldn11*-null (−/−; $n = 6$) mice. Scattering intensity is plotted against reciprocal coordinate R ($1/d$; $Å^{-1}$). Patterns have been offset along the y axis for clarity. Bragg orders are indicated with numerals above the reflections. (*B*) Scatter plots of relative amount of myelin ($M/[M+B]$) versus myelin period. Large colored symbols represent parameters measured from each mouse. Error bars represent ±1 standard deviation for myelin period and relative amount of myelin centered on the average for each group (*small colored symbols*). To see this figure in color, go online.

in both central and peripheral nervous system samples (Fig. 2 *B* and Table 1). This finding demonstrates a lack of overall structural changes in the absence of claudin-11 and supports the idea that the function of this protein is more specialized than that of simply providing adhesion or mechanical stability.

Membrane interactions are normal in *Cldn11*-null myelin

In the absence of any obvious structural defects in *Cldn11*-null myelin under physiological conditions, we subjected optic and sciatic nerves from +/+, +/−, and −/− mice to electrostatic stress followed by XRD analysis. Because myelin period is determined by the balance of attractive and repulsive forces between membrane surfaces, we hypothesized that equilibrating nerves against solutions of varied, nonphysiological ionic strength or pH might reveal

TABLE 1 Myelin structural parameters determined by x-ray diffraction

	Period (Å)	$M/(M+B)$	I_1/I_2	I_3/I_2	I_4/I_2	I_5/I_2	Slope	Intercept
Optic Nerve								
Cldn11 +/+ ($n = 3$)	156.8 ± 1.0	0.13 ± 0.04			0.40 ± 0.07		0.82 ± 0.29	323.7 ± 79.6
Cldn11 +/− ($n = 6$)	156.4 ± 0.4	0.13 ± 0.03			0.38 ± 0.04		0.92 ± 0.46	333.0 ± 54.6
Cldn11 −/− ($n = 6$)	156.7 ± 0.7	0.12 ± 0.03			0.37 ± 0.02		1.21 ± 0.46	351.2 ± 48.6
$p =$	0.72	0.85			0.64		0.39	0.76
Sciatic Nerve								
Cldn11 +/+ ($n = 3$)	175.8 ± 0.8	0.26 ± 0.07	0.014 ± 0.004	0.16 ± 0.005	0.58 ± 0.002	0.09 ± 0.01	0.18 ± 0.08	185.2 ± 38.0
Cldn11 +/− ($n = 6$)	176.2 ± 0.9	0.30 ± 0.07	0.021 ± 0.006	0.17 ± 0.02	0.55 ± 0.04	0.09 ± 0.01	0.17 ± 0.08	155.0 ± 38.3
Cldn11 −/− ($n = 6$)	176.1 ± 0.3	0.28 ± 0.05	0.018 ± 0.006	0.17 ± 0.02	0.57 ± 0.03	0.09 ± 0.01	0.16 ± 0.05	159.3 ± 44.5
$p =$	0.76	0.68	0.48	0.74	0.35	0.86	0.86	0.59

Statistical significance was measured using one-way analysis of variance. No significant differences were detected.

differences in membrane interactions between control and *Cldn11*-null CNS myelin, resulting in differences in period (30,35–37). When optic and sciatic nerves were incubated at pH 4 and physiological ionic strength, we observed a decrease in period; and, when these nerves were incubated at nonphysiological ionic strength (0.02 or 0.2) and pH 7.4, we observed an inverse dependence of myelin period on ionic strength (Fig. 3 *A*). These results are consistent with the well-characterized dependence of myelin period on pH and ionic strength (35). Of importance, however, myelin period between genotypes was indistinguishable in all experimental treatments.

In the absence of any major, observable differences between genotypes, we carried out a limited series of experiments on optic and sciatic nerves from only *Cldn11*-null mice wherein nerves were equilibrated at both nonphysiological pH (4 or 9.7) and nonphysiological ionic strength (0.02, 0.06, 0.15, or 0.2) (Fig. 3, *B* and *C*). These results were then compared to previously published work from WT mice on a different genetic background (35). Again, the expected trends in myelin period were observed: under nonphysiological conditions, period varied directly with pH and ionic strength; however, no differences were observed between knockout and control samples. These results indicate that membrane interactions in myelin are unaltered in the absence of claudin-11.

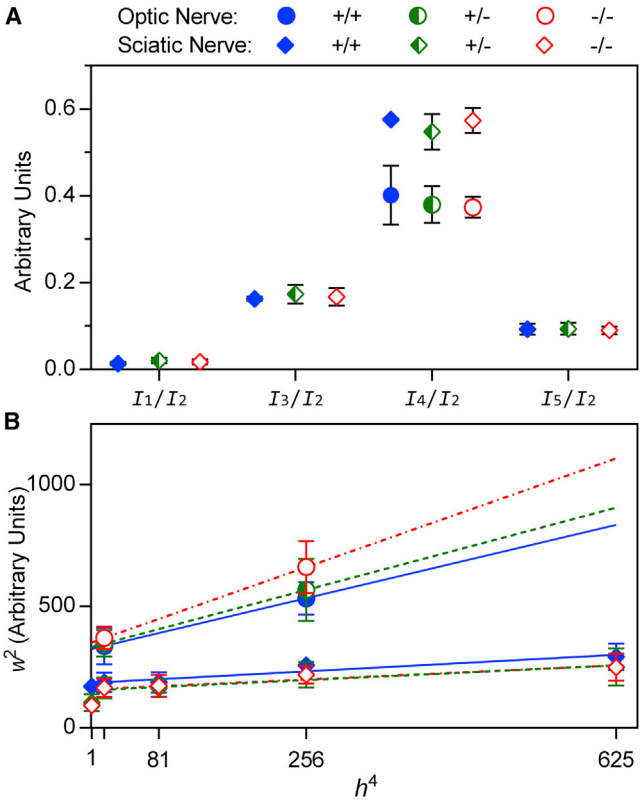

FIGURE 2 Myelin structure is unaltered in *Cldn11*-null mice. (*A*) Comparison between the relative intensities of Bragg reflections from optic and sciatic nerves. Intensities are expressed as the intensity of each reflection I_h of Bragg order h normalized to I_2. Symbols represent the averages for each genotype ±1 standard deviation. (*B*) The square of the full width at half-maximum for each reflection (w^2) is plotted against the Bragg order raised to the fourth power (h^4). Lines behind the points are linear least-squares fits for w^2 versus h^4 for each genotype. The slope of each line is directly related to the amount of disorder in myelin membrane packing, and the intercept is inversely related to the regularity of membrane packing (34). To see this figure in color, go online.

CNS myelin in *Cldn11*-null mice undergoes more rapid changes in period during osmotic stress

Because our XRD analysis did not uncover any differences in myelin structure in native or electrostatically stressed myelin, we compared the relative permeability of *Cldn11*-null myelin to that of control mice. Rather than using electrophysiological techniques, which typically measure the bulk electrical properties of myelinated tissue, or electron microscopy-based diffusion tracer methods, which are prone to tissue fixation and processing artifacts, we analyzed the diffraction from fresh tissue that was either equilibrated against or perfused with solutions containing small nonelectrolytes (e.g., glycerol, saccharides, polyethylene glycols (PEGs)) at concentrations expected to yield

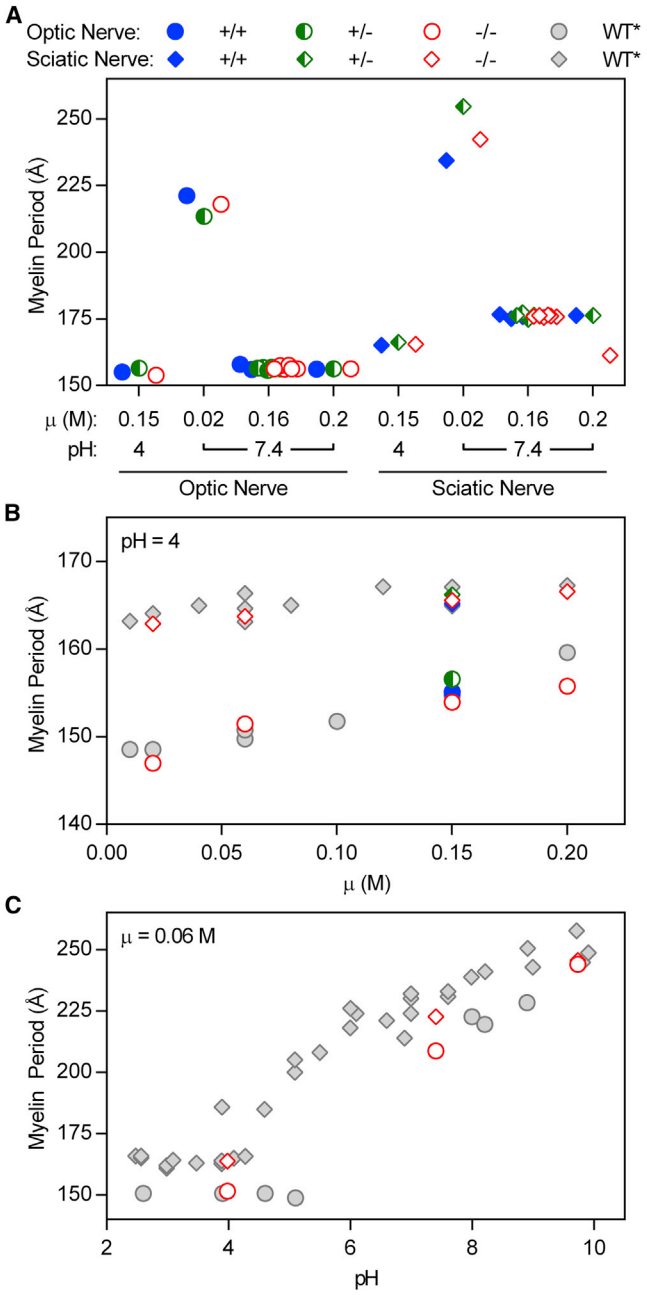

FIGURE 3 *Cldn11*-null myelin responds normally to electrostatic stress. (*A*) Myelin period was measured in WT, heterozygous, and *Cldn11*-null optic and sciatic nerves that were equilibrated against solutions of either nonphysiological pH or nonphysiological ionic strength. (*B* and *C*) Myelin period measured from nerves equilibrated against solutions of either (*B*) pH 4 and varying ionic strength or (*C*) low ionic strength and varying pH. *Gray symbols represent data from WT animals of a different genetic background (35). To see this figure in color, go online.

measurable changes in electron density of the aqueous compartments of multilamellar myelin (38).

Incubation with hyperosmotic nonelectrolytes caused significant, and sometimes transient, compaction of myelin. This effect was indistinguishable from the osmotic volume changes measured in erythrocytes and other model cells in hyperosmotic solutions, which have been widely used to study the permeability of membranes to various solutes (39). In myelin, the transience of compaction depended on the size of the osmotic agent: compaction was temporary for small osmolytes, but it was permanent when higher molecular weight osmolytes were used. For example, fresh nerves that were exposed to PEG 300 exhibited a native period after a brief equilibration time (Fig. S1 in the Supporting Material). However, when optic nerves were soaked in 0.45 M PEG 1450, the myelin rapidly compacted by ~35 Å and remained in this compacted state without recovery over the course of a 4-day treatment. When these same PEG 1450-treated nerves were placed in a solution containing the smaller and more permeant PEG 300 at the same molar concentration, myelin period rapidly returned to a native-like period. The inability of these nerves to completely return to their native state is most likely a result of the intense osmotic stress and duration of treatment. Of importance, some of the osmolytes that caused transient compaction in myelin (e.g., sucrose) are ones that are classically considered nonpenetrating solutes because of their inability to passively diffuse across plasma membranes, causing permanent shrinkage in erythrocytes and model liposomes (40–42). The reversible compaction of myelin during treatment with a membrane-impermeant solute suggests that diffusion is occurring through some other, more permissive barrier—i.e., the intramyelinic compartment and interlamellar TJs. By measuring the osmotic compaction and recovery of myelin, we might therefore be able to directly assess the contribution of the interlamellar TJs of the radial component to the permeability of the intramyelinic compartment. Indeed, osmotic stress (in conjunction with TEM) has been used to detect the presence of TJs between cells in other tissues (43,44).

To employ this approach, we perfused optic nerves from *Cldn11* +/+, +/−, and −/− mice with 1 M sucrose in physiological saline while collecting a tandem series of short XRD exposures (Fig. 4 *A*). Myelin period was determined by measuring the positions of the strong, second-order reflections at each time point. Upon perfusion, myelin period underwent an immediate compaction of 9.9 ± 0.9 Å ($n = 6$) during the first 10–20 min of the experiment. After reaching this minimum period, the compaction reversed, and myelin period increased toward its native value over the remainder of the experiment (>4 h). The compaction phase corresponds to the osmotic dehydration of myelin, whereas the recovery phase presumably represents the inward diffusion of water, sucrose, and salts (39). When the time courses of compaction and recovery of CNS myelin were compared between genotypes, we found significant differences between *Cldn11*-null and control (+/±; WT and heterozygous) mice. During the compaction phase, the change in period over time followed a one-phase exponential decay (Fig. S2). The relaxation time τ, or $t_{1/e}$, for this compaction in control samples was 5.97 ± 1.14 min ($n = 3$) compared to 2.70 ± 1.33 min

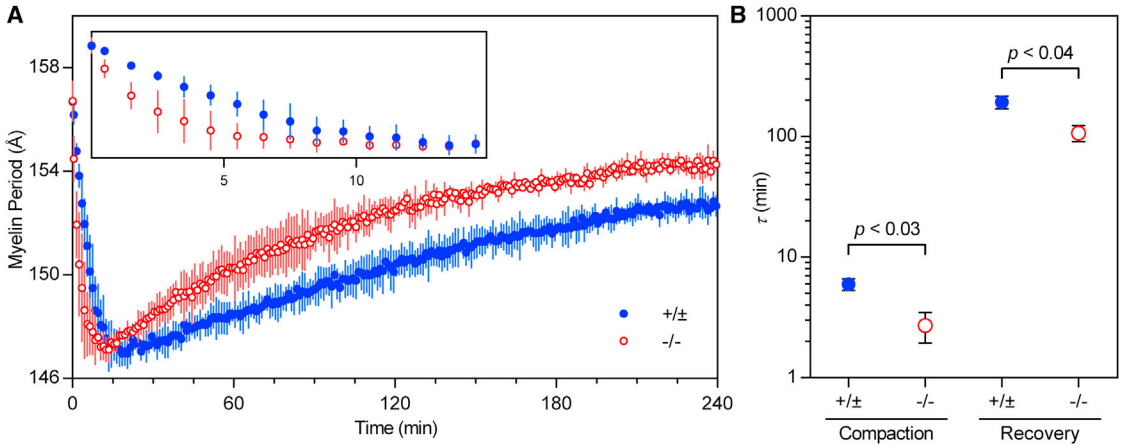

FIGURE 4 *Cldn11*-null myelin undergoes more rapid osmotic compaction and recovery. (*A*) Myelin period was measured in optic nerves from control (+/±) and *Cldn11*-null (−/−) mice while nerves were perfused with hyperosmotic sucrose. Points and error bars represent the average myelin period measured from $n = 3$ mice in each group at each time point ±1 standard deviation. For clarity, the inset shows an enlarged view of the first 15 min of the experiment. (*B*) Relaxation times τ were extracted from single-exponential decay models fit to plots of period versus time during osmotic compaction and recovery. Average relaxation times for each group are shown ±1 standard deviation. Statistical significance was calculated using a *t*-test between average relaxation times measured from control (+/±; $n = 3$) and *Cldn11*-null (−/−; $n = 3$) mice. To see this figure in color, go online.

($n = 3$) in samples from knockout mice (*t*-test, $p < 0.03$) (Fig. 4 *B*). The recovery phase also followed a one-phase exponential decay (Fig. S2). The relaxation times for recovery were 192.9 ± 40.9 min in control samples and 107.1 ± 27.4 min in knockout samples (*t*-test, $p < 0.04$) (Fig. 4 *B*). The shorter relaxation times for compaction and recovery in *Cldn11*-null myelin in these perfusion experiments correspond to a more rapid response to osmotic stress, suggesting increased rates of diffusion through the intramyelinic compartment in the absence of TJs.

Neutron diffraction measurements detect the absence of claudin-11

Because our XRD experiments suggest that claudin-11 serves as a diffusion barrier within the intramyelinic compartment, we next carried out complementary neutron diffraction experiments on *Cldn11*-null and control myelin. Unlike XRD, neutron diffraction is sensitive to the ratio between hydrogen and its heavy isotope deuterium in the sample. By collecting neutron diffraction patterns from myelinated tissues treated with buffers containing various concentrations of heavy water (D_2O), water exchange kinetics, the distribution of water, and other structural parameters can be determined (31,33). In preparation for eventual H_2O-D_2O exchange experiments, we soaked spinal cord segments from *Cldn11*-null and control mice in buffers containing either 43% or 100% D_2O and recorded their neutron diffraction patterns at equilibrium (Fig. 5 *A*). Consistent with our XRD findings, we found that the absence of claudin-11 had no effect on myelin period: control myelin had a period of 156.1 ± 0.9 Å ($n = 6$), whereas that of *Cldn11*-null myelin was 155.9 ± 1.1 Å ($n = 6$) (*t*-test, $p < 0.55$). Interestingly, when we compared the relative intensities of the reflections (I_h/I_2; normalized to the intensity of the major second-order reflection) between genotypes, we found that CNS myelin from *Cldn11*-null mice had a higher I_1/I_2 (0.121 ± 0.005; $n = 3$) than that from control mice (0.111 ± 0.002; $n = 3$) (*t*-test, $p < 0.03$) in 100% D_2O-saline (Fig. 5 *B*), indicating a greater asymmetry in neutron scattering density between the extracellular and cytoplasmic compartments. This difference most likely stems from the replacement of protein in the intramyelinic compartment with strongly scattering D_2O; the neutron scattering density for D_2O (0.63×10^{11} cm^{-2}) is significantly higher than that of deuterated protein (0.33×10^{11} cm^{-2}) (45). Moreover, when samples were equilibrated against 43% D_2O-saline, this difference in I_1/I_2 between groups disappeared, which was expected because the neutron scattering density of 43% D_2O approximates that of protein (46), thus eliminating any measurable contrast between claudin-11 and the water in the intramyelinic compartment.

Water diffuses more rapidly through CNS myelin in the absence of claudin-11

Finally, we used neutron diffraction to compare the rates of H_2O-D_2O exchange in CNS myelin from *Cldn11*-null and control mice. We hypothesized that if claudin-11 establishes a diffusion barrier within the intramyelinic compartment, then CNS myelin from *Cldn11*-null mice would show increased rates of water exchange. To test this, we equilibrated spinal cord segments from knockout and control mice against 20% D_2O-saline, loaded them into a flow chamber, and perfused them with 100% D_2O-saline while collecting serial neutron diffraction patterns. The extent of exchange was quantified by measuring the intensity of the strong second-order Bragg reflection over time (31,33)

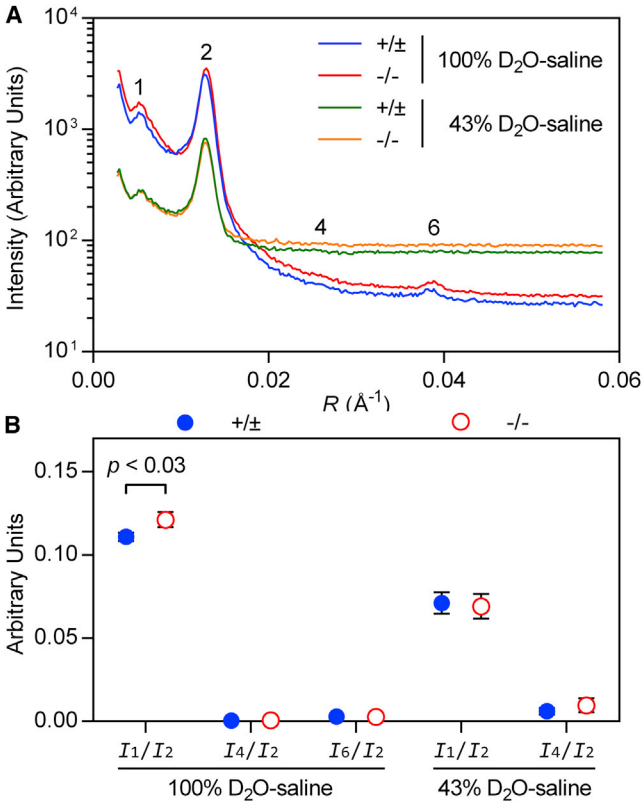

FIGURE 5 Neutron diffraction from *Cldn11*-null myelin reveals subtle changes in myelin structure. (*A*) Representative neutron diffraction patterns collected from spinal cords from control and *Cldn11*-null mice in either 100% or 43% D_2O-saline. Scattering intensity is plotted against reciprocal coordinate R ($1/d$; Å^{-1}). Bragg orders are indicated with numerals above the reflections. (*B*) Comparison of relative intensities of neutron reflections between spinal cords from control and *Cldn11*-null mice in 100% or 43% D_2O-saline. Symbols represent average relative intensities (I_h/I_2) of Bragg order h ± 1 standard deviation. Statistical significance was calculated using a *t*-test between average parameters measured from control (+/±; $n = 3$) and *Cldn11*-null (−/−; $n = 3$) mice. To see this figure in color, go online.

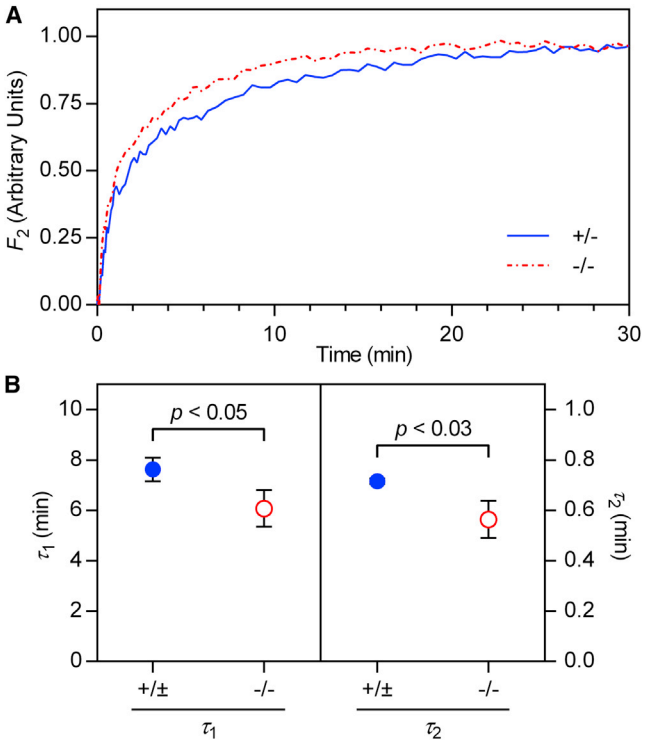

FIGURE 6 H_2O-D_2O exchange is more rapid in the absence of claudin-11. (*A*) Spinal cord segments from control and *Cldn11*-null mice were equilibrated against 20% D_2O-saline and then perfused with 100% D_2O-saline starting at $t = 0$. Each data series shows the observed second-order structure factor F_2 at each time point for representative experiments. F_2 has been scaled from 0 to 1 for clarity. (*B*) Relaxation times τ_1 and τ_2 were extracted from double-exponential decay models. Average relaxation times for each group are shown ± 1 standard deviation. Statistical significance was calculated using a one-tailed *t*-test between average relaxation times measured from control ($n = 6$) and *Cldn11*-null ($n = 5$) mice. To see this figure in color, go online.

(Fig. 6 *A*). We found that in both control and *Cldn11*-null samples, water exchange followed a double exponential decay, with a long, primary relaxation time (τ_1) and a shorter, secondary relaxation time (τ_2), which may correspond to different populations of exchangeable hydrogens within myelin (31). Relaxation times measured from control CNS samples ($n = 6$; τ_1, 7.48 ± 1.11 min; τ_2, 0.71 ± 0.03) were significantly longer than those measured from *Cldn11*-null samples ($n = 5$; τ_1, 5.76 ± 1.40 min; τ_2, 0.53 ± 0.15) (one-tailed *t*-test; τ_1, $p < 0.05$; τ_2, $p < 0.03$) (Fig. 6 *B*). As previously mentioned, the shorter relaxation times for *Cldn11*-null CNS myelin demonstrate increased rates of diffusion for water arising from the absence of interlamellar TJs.

DISCUSSION

In this study, we analyzed claudin-11-deficient CNS myelin to investigate the molecular function of myelin interlamellar TJs (radial component) and their contribution to nerve function. Many studies have demonstrated that claudins are the primary molecular species in TJs that regulate the diffusion of water and solutes through paracellular spaces (47). Claudin-11 in particular has been shown to have this property outside of the CNS; in the absence of claudin-11, the basal cells in the stria vascularis of the cochlea become permeable to horseradish peroxidase (27) and biotin (28) tracers despite the preservation of close cell-cell contacts and gap junction complexes (27). *Claudin 11*-null mice exhibit reduced CNS conduction velocity in auditory and visual pathways, a fine tremor, and hind limb weakness (1), and modeling of electrophysiology data from these mice shows that the observed nervous system deficits are consistent with an increase in current flow across the myelin sheath (2). However, direct evidence for a barrier defect in *Cldn11*-null CNS myelin had not yet been obtained.

In our investigations of the contribution of interlamellar TJs to myelin permeability, we avoided the use of electron microscopy and diffusion tracers, which have been widely

used in the study of myelin permeability (8–22). Although indispensable, these methods are prone to fixation and processing artifacts. Instead, we chose to use diffraction-based methods, which are inherently quantitative and can be performed on fresh, unfixed tissue, avoiding the artifacts associated with TEM (30,48–50). Using a combination of osmotic stress and XRD, we find that myelin undergoes osmotic compaction and recovery more rapidly in the absence of claudin-11, indicating that myelin is more accessible to water and small solutes in the absence of interlamellar TJs. Moreover, our measurements of H_2O-D_2O exchange in myelin using neutron diffraction show that the rate of diffusion of water into the intramyelinic compartment is greater in *Cldn11*-null myelin.

Together, our results herein show that the primary function of claudin-11 is to provide a barrier that impedes the diffusion of material through the intramyelinic compartment (Fig. 7). Claudin-11 is an essential constituent of the radial component of CNS myelin, an array of TJs that extends through the entire thickness of the sheath and, in mature myelin, is typically concentrated in the area between the inner and outer mesaxons (1,3,51,52). This limited distribution of the radial component to a narrow region of the sheath is consistent with the idea that its function is highly specialized and does not affect the properties of bulk membrane surfaces. Furthermore, because of its localization to the borders between the interstitial, intramyelinic, and periaxonal (submyelin) spaces, the radial component seems ideally situated to regulate diffusion into and out of myelin. This barrier most likely resists the formation of electrochemical gradients within the myelin sheath and, thereby, improves the passive properties of the membrane by increasing electrical resistance. Such an improvement would be most beneficial to small diameter axons, which harbor only a few wraps of membrane with relatively low resistance compared to large fibers. Of importance, these findings provide the molecular basis for previous electrophysiological and modeling experiments of myelin TJ function (2).

Still, a number of studies also suggest that the radial component may provide strong mechanical coupling between adjacent layers of myelin. Several groups have used conventional TEM to show that regions of the myelin sheath containing the radial component tend to remain compacted when myelin is subjected to hypotonic conditions (23) or hexachlorophene treatment (18). More recent work demonstrates a resistance to hypotonic swelling in aldehyde-fixed myelin lacking proteolipid protein (PLP), a major structural protein in CNS myelin (53). Despite these findings, strong adhesion is not a defining characteristic of canonical TJs. Although claudins are known to interact in *trans*, recent single-molecule studies have demonstrated relatively weak, transient adhesion between molecules of claudin-1 (another member of the claudin family) compared to that of bona fide adhesion proteins like E-cadherin (54). Some claudins are known to form atypical TJs such as the hybrid tight-adherens junctions with demonstrable adhesive properties in the organ of Corti (55); however, tight-adherens junctions have a markedly different morphology than that of TJs, particularly with respect to the presence of an adherens junction-like cytoplasmic plaque and association with an extensive cytoskeletal network, neither of which has been detected in myelin TJs. Furthermore, the lack of any detectable ultrastructural changes to myelin in *Cldn11*-null mice (beyond the absence of the radial component) seems inconsistent with any significant adhesive role (1,2,25,26).

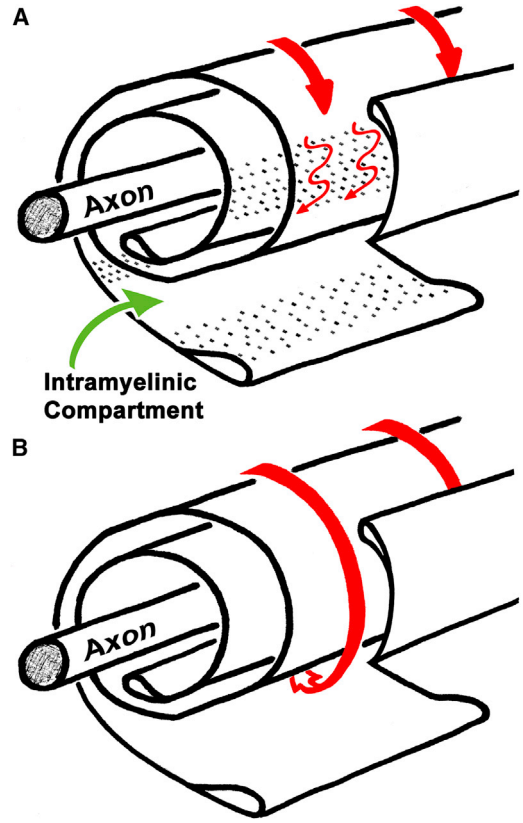

FIGURE 7 Claudin-11 TJs form a diffusion barrier in CNS myelin. (*A*) When a spiral of normal, multilayered CNS myelin is unraveled, claudin-11 TJs (*dots*) can be observed in the intramyelinic compartment. These TJs typically extend though the entire thickness of the sheath and, in mature myelin, are enriched in the region of the sheath between the inner and outer mesaxons. In the presence of these TJs, which span the intramyelinic compartment, this space is partially occluded, and diffusion (*red arrows*) through this space is obstructed. (*B*) In *Cldn11*-null tissue, myelin ultrastructure is unaltered, but CNS myelin TJs are absent. In the absence of these TJs, the intramyelinic compartment is more accessible, and diffusion occurs more rapidly. To see this figure in color, go online.

Although it seems unlikely that claudin-11 has significant adhesive properties, *Cldn11*-null myelin has only been examined using TEM, which is susceptible to fixation artifacts that can alter myelin structure (30,48–50). To investigate the adhesiveness of claudin-11 TJs, we compared myelin structure in fresh, unfixed tissue from control and *Cldn11*-null mice using XRD. Our initial XRD analysis of

Cldn11-null CNS myelin under physiological conditions demonstrated that the absence of claudin-11 caused no detectable changes in the amount of myelin, myelin period, membrane packing disorder, crystallinity, or the distribution of electron density across the repeating unit (pair of bilayers). Considering the possibility that perturbations in myelin structure could be masked under physiological conditions, we hypothesized that differences in membrane packing could be revealed by electrostatically stressing the myelin before XRD (30,35,36). In fact, several of the previous studies that suggested an adhesive role for claudin-11 used osmotic and electrostatic stress to induce separation at myelin's extracellular apposition (23,53). We equilibrated nerves against solutions of nonphysiological pH and/or ionic strength to uncover differences in myelin membrane interactions manifesting as an altered period. Again, knockout and control samples were indistinguishable under all conditions, indicating that claudin-11 does not contribute significantly to the adhesive properties of myelin membranes, consistent with earlier TEM studies of *Cldn11*-null myelin (1,2,25,26).

How do we reconcile the apparent adhesiveness of the radial component reported in several previous studies of osmotically or chemically stressed myelin with the lack of structural defects in myelin lacking claudin-11 observed herein and elsewhere? It is important to consider that in the work performed with *Plp1*-null myelin, the tissue was fixed before the application of osmotic stress (53). Even in mice lacking both PLP and claudin-11, which together comprise the majority of the protein at the extracellular apposition, compact (albeit loosely wrapped), multilamellar myelin is formed (26). In the absence of only PLP, claudin-claudin *trans*-interactions are therefore, as expected, cross-linked during aldehyde fixation. Osmotic stress is not sufficient to disrupt chemical cross-links; thus, the TJ-containing regions of the sheath remain associated, whereas those lacking TJs swell apart, giving the radial component the appearance of providing mechanical stability.

Earlier researchers fixed WT tissue after subjecting it to either a hypotonic solution (23) or hexachlorophene treatment (18). Although the radial component was free to separate during treatment, these studies are still unconvincing. In the case of hexachlorophene-treated WT nerves, splitting of lamellae was rare, and TJ-free regions of the sheath remained largely compacted (18). When WT rodent nerves were soaked in hypotonic solutions, the intact myelin that persisted after treatment almost always contained the radial component (23). Although, again, complete separation of lamellae was rare, and even the swollen TJ-free regions of the sheath swelled in units of four membranes (i.e., at alternating extracellular appositions). Although it is conceivable that TJs may contribute to the stability of the intact regions, this striking swelling behavior of CNS myelin observed by these and other authors demonstrates the presence of robust, TJ-independent adhesion in CNS myelin (56–61). In fact, even purified myelin lipids or white matter lipids are capable of forming compact multilamellar structures in vitro with or without added protein (62–64). Therefore, it is likely that the apparent resistance to swelling of the radial component is the result of the combined effects of TJ-independent adhesion and transient interactions between TJ proteins on dynamic, undulating membranes, which are made permanent upon aldehyde-fixation. If claudin-11 does, in fact, provide mechanical stability, the effect may be subtle and secondary to other stronger adhesive mechanisms in normal myelin. Rather, our work directly demonstrates that the primary function of claudin-11 is to hinder the diffusion of material through the myelin sheath.

SUPPORTING MATERIAL

Two figures are available at http://www.biophysj.org/biophysj/supplemental/S0006-3495(15)00823-1.

AUTHOR CONTRIBUTIONS

A.R.D., A.B., B.D., A.G., and D.A.K. designed experiments; A.R.D., A.B., K.J.M., G.L., V.C., B.D., and D.A.K. carried out experiments; A.R.D., A.B., V.C., B.D., and D.A.K. analyzed data; A.R.D., A.G., and D.A.K. wrote the article.

ACKNOWLEDGMENTS

We thank Adrian Perkins and Didier Richard at the ILL and Dominique Dallery, Charlene Caloud, and Helene Bernard at the ESRF for experimental support. We also thank Brian White, Perry Nuckle, and W. Bruce Feller at NOVA Scientific Inc. (Sturbridge, MA) and Paul Dee at Boston College for designing and fabricating the perfusion cells. We are grateful to Dr. G. Zaccai for his encouragement of this research.

This research was supported by the Fondation pour l'Aide à la Recherche sur la Sclérose en Plaques (ARSEP Foundation; to D.A.K.), L'Association Européenne contre les Leucodystrophies – ELA (ELA Foundation, grant Nos. ELA2008-009C4 and ELA2010-042C5; to D.A.K.), Boston College Institutional Research Funds (to D.A.K.), the Burroughs Wellcome Fund (Collaborative Research Travel Grant; to A.R.D.), the National Institutes of Health, NIDCD (DC006262; to A.G.), the National Multiple Sclerosis Society (RG4639; to A.G.) and the Carls Foundation of Michigan (to A.G.).

REFERENCES

1. Gow, A., C. M. Southwood, …, R. A. Lazzarini. 1999. CNS myelin and sertoli cell tight junction strands are absent in Osp/claudin-11 null mice. *Cell.* 99:649–659.
2. Devaux, J., and A. Gow. 2008. Tight junctions potentiate the insulative properties of small CNS myelinated axons. *J. Cell Biol.* 183:909–921.
3. Peters, A. 1961. A radial component of central myelin sheaths. *J. Biophys. Biochem. Cytol.* 11:733–735.
4. Honjin, R. 1959. Electron microscopic studies on the myelinated nerve fibers in the central nervous system. *Acta Anat. Nippon.* 34:43–44, (Abstr.).
5. Farquhar, M. G., and G. E. Palade. 1963. Junctional complexes in various epithelia. *J. Cell Biol.* 17:375–412.
6. Friend, D. S., and N. B. Gilula. 1972. Variations in tight and gap junctions in mammalian tissues. *J. Cell Biol.* 53:758–776.

7. Goodenough, D. A., and J. P. Revel. 1970. A fine structural analysis of intercellular junctions in the mouse liver. *J. Cell Biol.* 45:272–290.
8. Hirano, A., N. H. Becker, and H. M. Zimmerman. 1969. Isolation of the periaxonal space of the central myelinated nerve fiber with regard to the diffusion of peroxidase. *J. Histochem. Cytochem.* 17:512–516.
9. Hirano, A., and H. M. Dembitzer. 1969. The transverse bands as a means of access to the periaxonal space of the central myelinated nerve fiber. *J. Ultrastruct. Res.* 28:141–149.
10. Revel, J. P., and D. W. Hamilton. 1969. The double nature of the intermediate dense line in peripheral nerve myelin. *Anat. Rec.* 163:7–15.
11. Klemm, H. 1970. [The perineurium: a diffusion barrier for peroxidase in epineurial and endoneurial application]. *Z. Zellforsch. Mikrosk. Anat.* 108:431–445.
12. Feder, N. 1971. Microperoxidase. An ultrastructural tracer of low molecular weight. *J. Cell Biol.* 51:339–343.
13. Hall, S. M., and P. L. Williams. 1971. The distribution of electron-dense tracers in peripheral nerve fibres. *J. Cell Sci.* 8:541–555.
14. Luft, J. H. 1971. Ruthenium red and violet. II. Fine structural localization in animal tissues. *Anat. Rec.* 171:369–415.
15. Reier, P. J., T. Tabira, and H. D. Webster. 1976. The penetration of fluorescein-conjugated and electrondense tracer proteins into *Xenopus* tadpole optic nerves following perineural injection. *Brain Res.* 102:229–244.
16. Towfighi, J., and N. Gonatas. 1977. The distribution of peroxidases in the sciatic nerves of normal and hexachlorophene intoxicated developing rats. *J. Neurocytol.* 6:39–47.
17. Reier, P. J., T. Tabira, and Hd. Webster. 1978. Hexachlorophene-induced myelin lesions in the amphibian central nervous system. A freeze-fracture study. *J. Neurol. Sci.* 35:257–274.
18. Tabira, T., M. J. Cullen, …, H. deF. Webster. 1978. An experimental analysis of interlamellar tight junctions in amphibian and mammalian C.N.S. myelin. *J. Neurocytol.* 7:489–503.
19. Shivers, R. R. 1979. Occluding-like junctions at mesaxons of central myelin in *Anolis carolinensis* are not 'tight'. A freeze-fracture-protein tracer analysis. *Tissue Cell.* 11:353–358.
20. Dermietzel, R., A. G. Leibstein, and D. Schünke. 1980. Interlamellar tight junctions of central myelin. II. A freeze fracture and cytochemical study on their arrangement and composition. *Cell Tissue Res.* 213: 95–108.
21. MacKenzie, M. L., M. N. Ghabriel, and G. Allt. 1984. Nodes of Ranvier and Schmidt-Lanterman incisures: an in vivo lanthanum tracer study. *J. Neurocytol.* 13:1043–1055.
22. Mackenzie, M. L., Z. Shorer, …, G. Allt. 1984. Myelinated nerve fibres and the fate of lanthanum tracer: an in vivo study. *J. Anat.* 138:1–14.
23. McIntosh, T. J., and J. D. Robertson. 1976. Observations on the effect of hypotonic solutions on the myelin sheath in the central nervous system. *J. Mol. Biol.* 100:213–217.
24. Morita, K., H. Sasaki, …, S. Tsukita. 1999. Claudin-11/OSP-based tight junctions of myelin sheaths in brain and Sertoli cells in testis. *J. Cell Biol.* 145:579–588.
25. Chow, E., J. Mottahedeh, …, J. M. Bronstein. 2005. Disrupted compaction of CNS myelin in an OSP/Claudin-11 and PLP/DM20 double knockout mouse. *Mol. Cell. Neurosci.* 29:405–413.
26. Devaux, J., B. Fykkolodziej, and A. Gow. 2010. Claudin proteins and neuronal function. *Curr. Top. Membr.* 65:229–253.
27. Gow, A., C. Davies, …, B. Kachar. 2004. Deafness in Claudin 11-null mice reveals the critical contribution of basal cell tight junctions to stria vascularis function. *J. Neurosci.* 24:7051–7062.
28. Kitajiri, S., T. Miyamoto, …, S. Tsukita. 2004. Compartmentalization established by claudin-11-based tight junctions in stria vascularis is required for hearing through generation of endocochlear potential. *J. Cell Sci.* 117:5087–5096.
29. Mazaud-Guittot, S., E. Meugnier, …, B. Le Magueresse-Battistoni. 2010. Claudin 11 deficiency in mice results in loss of the Sertoli cell epithelial phenotype in the testis. *Biol. Reprod.* 82:202–213.
30. Avila, R. L., H. Inouye, …, D. A. Kirschner. 2005. Structure and stability of internodal myelin in mouse models of hereditary neuropathy. *J. Neuropathol. Exp. Neurol.* 64:976–990.
31. Denninger, A. R., B. Demé, …, D. A. Kirschner. 2014. Neutron scattering from myelin revisited: bilayer asymmetry and water-exchange kinetics. *Acta Crystallogr. D Biol. Crystallogr.* 70:3198–3211.
32. ILL. Neutrons for science: Data analysis. http://www.ill.eu/instruments-support/computing-for-science/data-analysis. Accessed May 31, 2011.
33. Kirschner, D. A., D. L. Caspar, …, A. C. Nunes. 1976. Neutron diffraction studies of nerve myelin. *Brookhaven Symp. Biol.* (27):III68–III76.
34. Inouye, H., J. Karthigasan, and D. A. Kirschner. 1989. Membrane structure in isolated and intact myelins. *Biophys. J.* 56:129–137.
35. Inouye, H., and D. A. Kirschner. 1988. Membrane interactions in nerve myelin. I. Determination of surface charge from effects of pH and ionic strength on period. *Biophys. J.* 53:235–245.
36. Avila, R. L., M. D'Antonio, …, D. A. Kirschner. 2010. P0 (protein zero) mutation S34C underlies instability of internodal myelin in S63C mice. *J. Biol. Chem.* 285:42001–42012.
37. Karthigasan, J., E. L. Evans, …, D. A. Kirschner. 1996. Effects of rumpshaker mutation on CNS myelin composition and structure. *J. Neurochem.* 66:338–345.
38. Blaurock, A. E. 1971. Structure of the nerve myelin membrane: proof of the low-resolution profile. *J. Mol. Biol.* 56:35–52.
39. Sha'afi, R. I., and C. M. Gary-Bobo. 1973. Water and nonelectrolytes permeability in mammalian red cell membranes. *Prog. Biophys. Mol. Biol.* 26:103–146.
40. Teorell, T. 1952. Permeability properties of erythrocyte ghosts. *J. Gen. Physiol.* 35:669–701.
41. Selser, J. C., Y. Yeh, and R. J. Baskin. 1976. A light-scattering measurement of membrane vesicle permeability. *Biophys. J.* 16:1357–1371.
42. Bangham, A. D., J. De Gier, and G. G. Greville. 1967. Osmotic properties and water permeability of phospholipid liquid crystals. *Chem. Phys. Lipids.* 1:225–246.
43. Russell, L. D., A. Bartke, and J. C. Goh. 1989. Postnatal development of the Sertoli cell barrier, tubular lumen, and cytoskeleton of Sertoli and myoid cells in the rat, and their relationship to tubular fluid secretion and flow. *Am. J. Anat.* 184:179–189.
44. Willems, A., S. R. Batlouni, …, G. Verhoeven. 2010. Selective ablation of the androgen receptor in mouse sertoli cells affects sertoli cell maturation, barrier formation and cytoskeletal development. *PLoS One.* 5:e14168.
45. Kirschner, D. A. 1974. Comparative x-ray and neutron diffraction from nerve myelin membranes. *In* Spectroscopy in Biology and Chemistry. S. Yip and S. H. Chen, editors. Academic Press, NY., pp. 203–233.
46. Jacrot, B. 1976. The study of biological structures by neutron scattering from solution. *Rep. Prog. Phys.* 39:911–953.
47. Van Itallie, C. M., and J. M. Anderson. 2006. Claudins and epithelial paracellular transport. *Annu. Rev. Physiol.* 68:403–429.
48. Moretz, R. C., C. K. Akers, and D. F. Parsons. 1969. Use of small angle x-ray diffraction to investigate disordering of membranes during preparation for electron microscopy. I. Osmium tetroxide and potassium permanganate. *Biochim. Biophys. Acta.* 193:1–11.
49. Moretz, R. C., C. K. Akers, and D. F. Parsons. 1969. Use of small angle x-ray diffraction to investigate disordering of membranes during preparation for electron microscopy. II. Aldehydes. *Biochim. Biophys. Acta.* 193:12–21.
50. Kirschner, D. A., and C. J. Hollingshead. 1980. Processing for electron microscopy alters membrane structure and packing in myelin. *J. Ultrastruct. Res.* 73:211–232.
51. Nagara, H., and K. Suzuki. 1981. Radial component of central myelin in normal and quaking mice. *Neuropathol. Appl. Neurobiol.* 7:151–160.
52. Kosaras, B., and D. A. Kirschner. 1990. Radial component of CNS myelin: junctional subunit structure and supramolecular assembly. *J. Neurocytol.* 19:187–199.

53. Rosenbluth, J., R. Schiff, and P. Lam. 2009. Effects of osmolality on PLP-null myelin structure: implications re axon damage. *Brain Res.* 1253:191–197.

54. Lim, T. S., S. R. Vedula, …, C. T. Lim. 2008. Single-molecular-level study of claudin-1-mediated adhesion. *Langmuir.* 24:490–495.

55. Nunes, F. D., L. N. Lopez, …, B. Kachar. 2006. Distinct subdomain organization and molecular composition of a tight junction with adherens junction features. *J. Cell Sci.* 119:4819–4827.

56. Finean, J. B., and R. E. Burge. 1963. The determination of the fourier transform of the myelin layer from a study of swelling phenomena. *J. Mol. Biol.* 7:672–682.

57. Lalitha, S., and C. R. Worthington. 1975. The swelling property of central nervous system nerves using x-ray diffraction. *J. Mol. Biol.* 96:625–639.

58. Autilio, L. A., W. T. Norton, and R. D. Terry. 1964. The preparation and some properties of purified myelin from the central nervous system. *J. Neurochem.* 11:17–27.

59. Linington, C., and M. G. Rumsby. 1980. Accessibility of galactosyl ceramides to probe reagents in central nervous system myelin. *J. Neurochem.* 35:983–992.

60. Wolfgram, F., and K. Kotorii. 1968. The composition of the myelin proteins of the central nervous system. *J. Neurochem.* 15:1281–1290.

61. Sedzik, J., A. D. Toews, …, P. Morell. 1984. Resistance to disruption of multilamellar fragments of central nervous system myelin. *J. Neurochem.* 43:1415–1420.

62. Franks, N. P., V. Melchior, …, D. L. Caspar. 1982. Structure of myelin lipid bilayers. Changes during maturation. *J. Mol. Biol.* 155:133–153.

63. Brown, 3rd, F. R., J. Karthigasan, …, D. A. Kirschner. 1989. X-ray diffraction analysis of myelin lipid/proteolipid protein multilayers. *J. Neurosci. Res.* 24:192–200.

64. Riccio, P., A. Fasano, …, D. A. Kirschner. 2000. Multilamellar packing of myelin modeled by lipid-bound MBP. *J. Neurosci. Res.* 59:513–521.

Claudin-11 tight junctions in myelin are a barrier to diffusion and lack strong adhesive properties

A.R. Denninger, A. Breglio, K.J. Maheras, G. LeDuc, V. Cristiglio, B. Demé, A. Gow, and D.A. Kirschner

Supporting Material

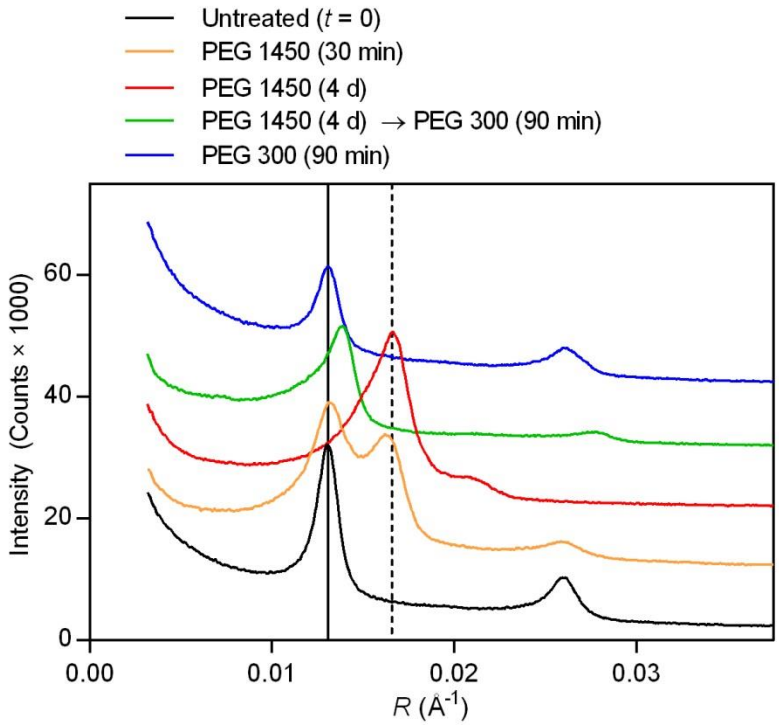

Figure S1. **Reversible compaction of CNS myelin.** X-ray diffraction patterns collected from wild-type optic nerves treated with PEG 1450 and/or PEG 300 for various lengths of time. Scattering intensity is plotted against reciprocal coordinate R ($Å^{-1}$). Patterns have been offset along the y axis for clarity. Vertical lines represent the positions of the second-order reflection for native (*solid*) and compacted (*dashed*) myelin.

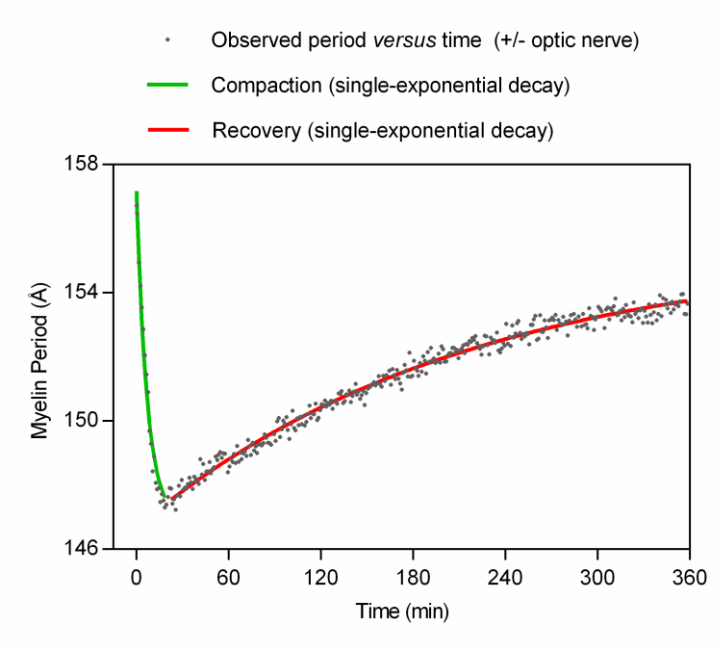

Figure S2. **Modeling of reversible compaction and recovery.** Symbols show the observed myelin period at each timepoint during a typical sucrose perfusion experiment. The green and red lines represent single-exponential decay models that were fit to the compaction and recovery phases of the experiment, respectively.